Additively manufactured degradable piezoelectric microsystems for sensing and actuating

Morgan M. Monroe, Nicolas Fumeaux, L. Guillermo Villanueva, Danick Briand*

M. Monroe, N. Fumeaux, D. Briand

Soft Transducers Laboratory, Institute of Mechanical Engineering

École Polytechnique Fédérale de Lausanne (EPFL)

Rue de la Maladière 71b, CH-2000 Neuchâtel, Switzerland

E-mail: danick.briand@epfl.ch

L. G. Villanueva

Advanced NEMS Laboratory, Institute of Mechanical Engineering

École Polytechnique Fédérale de Lausanne (EPFL)

1015 Lausanne, Switzerland

The global overabundance of electronic waste and concerns regarding energy- and material-intensive processes associated with traditional electronics manufacturing is driving the development of solution-processed, degradable electronics. In particular, printed degradable piezoelectrics have widespread potential to replace industry-dominant Pb-based devices used in many transducing applications. Yet current eco-friendly multi-material printing processes are limited by both the conventional challenges of multilayer process integration and the low-temperature thermal constraints of biodegradable materials. In this study, we present a novel approach to fabricating additively manufactured sustainable piezoelectric devices made with degradable electrode materials on paper substrates. The screen-printed, eco-friendly $KNbO_3$ piezoelectric transducers are combined with degradable carbon- or zinc-based conductive inks. We evaluate physical, dielectric, and piezoelectric device properties, assessing the influence of electrode material on performance. We report effective piezoelectric coefficients as high as 4.6 pC N^{-1} and 5.1 pC N^{-1} for printed devices with carbon and zinc electrodes

respectively. We then demonstrate the developed technology in sensing and actuating applications, presenting the first instance of sustainable fully additively manufactured piezoelectric force sensors and acoustic speakers. In demonstrating entirely printable piezoelectric devices compatible with various green electrode materials, we work to develop more complex sustainable printed piezoelectric technologies in the future.

1. Introduction

The global overabundance of electronic waste (e-waste) is a growing issue worldwide, with particular concerns related to the industry-wide dependence on non-renewable and environmentally toxic electronic materials.[1–3] Further concerns have been raised regarding the energy and material-intensive processes traditionally implemented for traditional electronics manufacturing via microfabrication. Thus, the rising demand for sustainable and eco-friendly technologies has led to the developing field of additively manufactured biodegradable electronics, where researchers are actively working to address both material and fabrication environmental issues associated with conventional electronics.[4–7]

Among the various types of electronics, piezoelectric devices have gained significant attention in recent years for their diverse range of sensing and actuating applications resulting from their transduce properties. The current dominance of this industry by materials such as the lead-containing lead zirconate titanate (PZT) and its derivatives motivates the transition to eco-friendly piezoelectrics and particularly away from the energy-intensive manufacturing processes typically required for perovskite ceramic ferroelectrics.[8,9]

Additive manufacturing is advantageous for applications in which scalability, cost-effectiveness, and low material waste are preferred.[10,11] However, the development of new printed materials requires optimization of printable ink formulations, deposition processes, and post-treatment methods to achieve the desired functionalities while minimally influencing the adjacent device materials (e.g. substrates or other functional materials) or compromising the performance of the target material.[6,12–15] Of note in this regard is process challenges associated with biodegradable substrates, such as paper or silk. These materials have low thermal budgets and are generally unable to withstand processes over 250 °C.[16,17] As such, eco-friendly multi-material printing processes are entirely constrained to the low-temperature regime.

Printing of green electronics has experienced great progress in recent years, particularly for systems containing a single printed functional material. In particular, processes for printing conductive (e.g. Zn, Mo, carbon) materials have been developed for integration with green substrates, with tailored processes for the printing and post-treatment that are often unique to each specific material.[6,7,18–20] Yet the applicability of devices composed of a single conductive layer are limited, and thus driving the initiative to merge these printed technologies with more specialized functional materials. Meanwhile, work on printed degradable piezoelectrics compatible with green substrates has only recently progressed, with Monroe having recently developed an ink appropriate for low temperature screen printing of piezoelectric $KNbO_3$ (KN) compatible with paper substrates for the first time, utilizing thermally evaporated gold layers as electrodes.[8,21] As currently stands, the manufacture of fully printed piezoelectric devices comprised entirely of degradable materials remains a significant challenge, and acts as an obstacle in the development of higher complexity sustainable printed electronics.[6]

In this study, we present a novel approach to the fabrication of fully additively manufactured and degradable piezoelectric devices on paper. We look to integrate the recently established printed $KNbO_3$ process with printed degradable conductors in the form of carbon or zinc-based inks. We further exploited the potential of the developed technology by fabricating sensing and actuating devices. While carbon inks have been the standard for many biodegradable electronics applications, their poor conductivity makes them non-ideal for widespread industrial use.[22,23] Conversely, zinc based conductive layers show remarkably better electrical performance relative to carbon, but in order to produce long-lifetime conductive layers, a multi-step hybrid sintering process should be implemented (as recently described by Fumeaux).[24] This combined electrochemical and photonic sintering procedure makes process integration into multi-material printed devices significantly more challenging. However, both zinc and carbon based printed conductive layers show great promise for integration into eco-friendly fully printed piezoelectric devices.

We look to evaluate the viability of an integrated printing process for piezoelectric devices using either electrode material, and assess the challenges and device characteristics achievable with either material. We evaluate the physical, dielectric, and piezoelectric properties of the devices, with focus on the influence of the two electrode materials on device performance. We also demonstrate the integration of these devices into sensing and actuating applications

in the form of touch sensors and acoustic speakers, highlighting their potential for use in sustainable microsystems by taking advantage of both the direct and inverse piezoelectric capabilities of the printed devices.

2. Results and Discussion

2.1. Process Development

All devices fabricated for primary assessment followed a consistent fabrication procedure, with variance only in the processing of the electrode materials, as depicted in **Figure 1**(a). These devices were based on a parallel place capacitor architecture with effective surface areas of 5, 10, 20, 30, and 60 mm^2 (Figure 1(d)). A sandwich configuration was selected to avoid any potential step-coverage related issues coming from the printed bottom electrode layers. Carbon layers were printed using a commercial ink, while the zinc and piezoelectric KN inks were mixed in-house according to previously established recipes (See Methods for details).

The following process was implemented for the fabrication of fully printed piezoelectric devices. First, bottom electrodes were deposited onto a paper substrate. For carbon and zinc inks, electrodes were screen printed onto the substrate. Carbon electrodes were cured in ambient conditions for 12 hrs. Zinc electrodes were cured using the hybrid sintering process developed by Fumeaux, which will be discussed in the following paragraphs.[24] For the reference samples, a 10/100 nm Cr/Au layer was deposited via thermal evaporation, following previous work on this system.[21]

Once the bottom electrodes were deposited and cured, the piezoelectric film was screen-printed onto all devices. Each layer of KN ink was cured for 30 min at 120 °C in an oven. To ensure a sufficiently high yield of viable devices, six layers of KN were printed for a total KN film thickness of approximately 30 μm, thereby preventing shorts between the electrodes. Finally, top electrodes were deposited following the same processes used for the bottom electrodes, resulting in piezoelectric capacitor devices with either both electrodes composed of carbon-based conductors ("carbon electrode") or both composed of zinc-based conductors ("zinc electrode"). All parameters were maintained for the top electrode processing with the exception of the sintering parameters for the zinc printed layers.
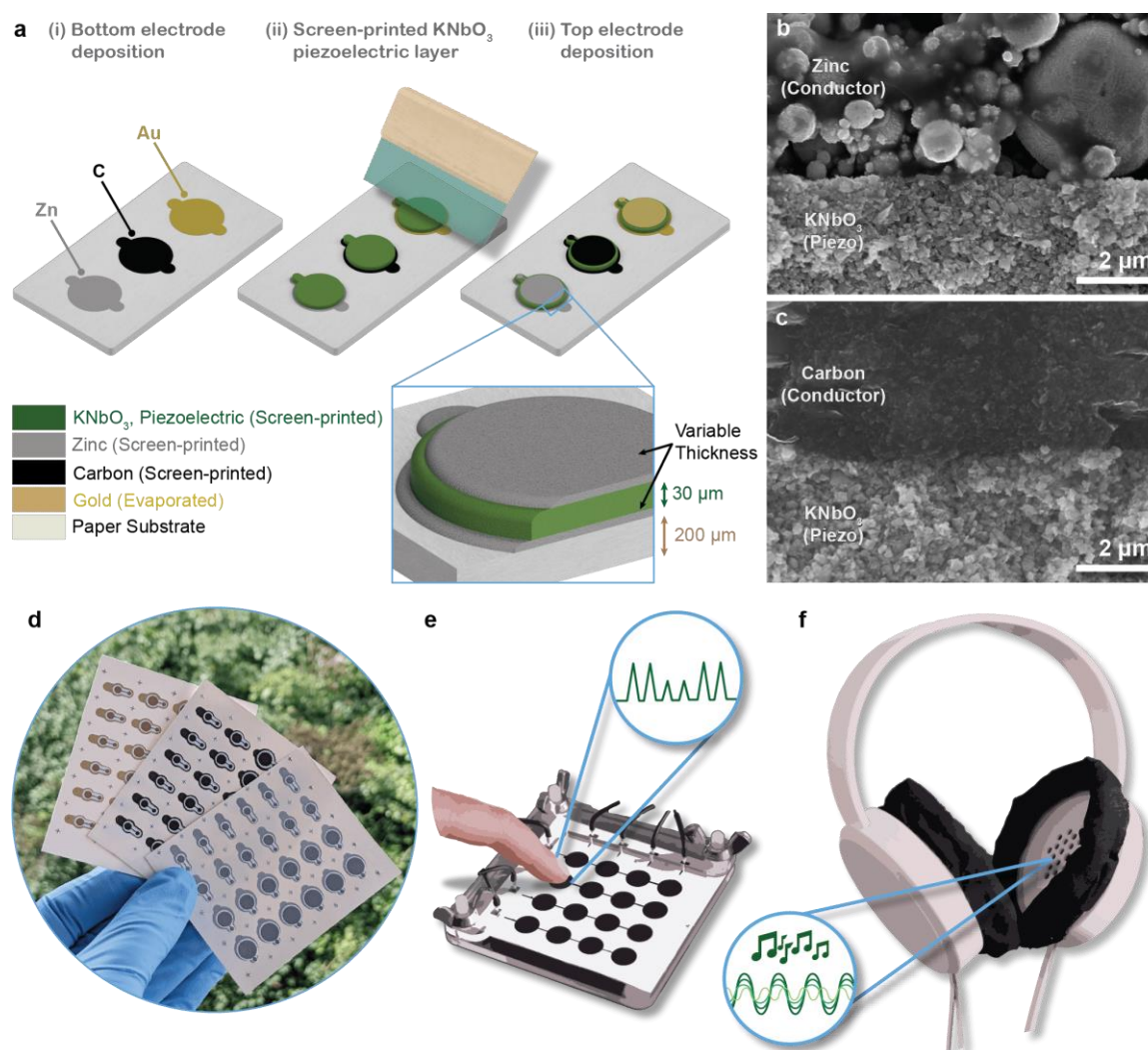
Figure 1. Overview of this work. a) Simplified process diagram showing the electrode materials under evaluation, printed zinc or carbon, as compared to conventional evaporated gold electrodes. The piezoelectric has been colored green for visibility. b) SEM image of the zinc-KN and c) Carbon-KN interfaces. d) Photographic image showing as-printed devices of varying electrode materials and capacitor sizes. e) Stylized drawing of the fabricated degradable touch sensor grid demonstrator detailed in this work. f) Stylized drawing of the fabricated degradable headphone demonstrator detailed in this work.

Prior work by Fumeaux has established a two-step treatment process for producing conductive layers of printed zinc that is compatible with paper substrates (described schematically in Supporting Information Figure S1.1).[24] First, aerosolized acetic acid is used to reduce the native oxide layer on the zinc particles, then photonic sintering is used to agglomerate the zinc particles before re-oxidation can occur. As the efficacy of photonic sintering is dependent on the thermal properties of the device stack being exposed, sintering parameters must be determined separately for the top and bottom zinc electrode layers. A protocol consisting of three 6550 mJ cm^{-2} pulses of 30 ms duration at a pulse frequency of 0.1 Hz was developed for screen printed zinc electrodes on paper substrates, directly applicable

5

for the bottom electrode zinc layers in this work. As such, it remains to determine effective sintering parameters for the top electrode zinc layer, as the thermal characteristics of the system changes from that of the bottom electrode with the addition of further device layers. Critically, the sintering parameters for the top electrode layer must produce conductive layers of zinc, but not compromise the integrity of the stack below.

With all other conditions fixed, the pulse energy and the number of pulses imparted on the devices was varied. **Figure 2** shows photographically the effects of varying these parameters on the device stack (with more detailed information available in Supporting Information Figure S1.2 and Figure S1.3). A combination of visual inspection and electrode conductivity evaluation was used to identify ideal sintering parameters. From this, it was determined that one pulse of 7550 mJ cm^{-2} was ideal with regards to sintering of top electrode zinc for this process.[24]
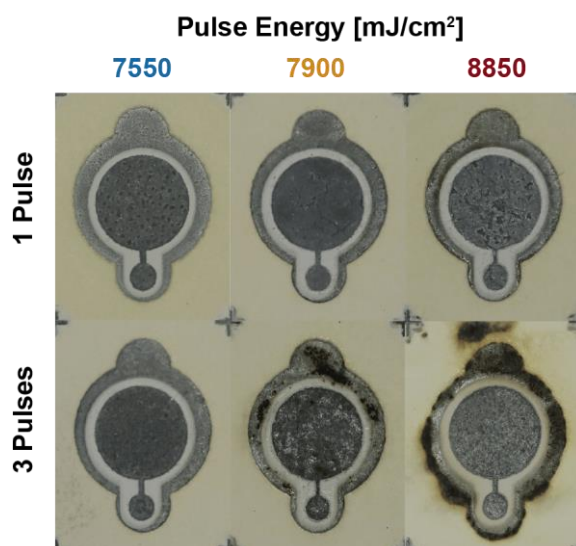

Figure 1. Zinc post-printing sintering process development. Photographic depiction of the influence of photonic sintering parameter on the printed layer stack, as used for the determination of ideal process parameters.

2.2. Influence of Electrode Material on Device Properties

2.2.1. Physical Characteristics

The final completed devices were first evaluated for their physical properties. Profilometry was used to evaluate the surface roughness and thickness of each printed layer. Representative profilometry data is shown in **Figure 3**(a) for devices printed on paper substrates with (i) zinc and (ii) carbon electrodes. As the high initial surface roughness of the paper substrates (2-3 µm) made measurement of individual layer thicknesses challenging, measurements were confirmed by comparison to samples printed on glass substrates (average roughness < 5 nm),

which are included in Supporting Information Figure S2.1 and Figure S2.2, all values reported in the following discussion were measured for samples printed on paper substrates.
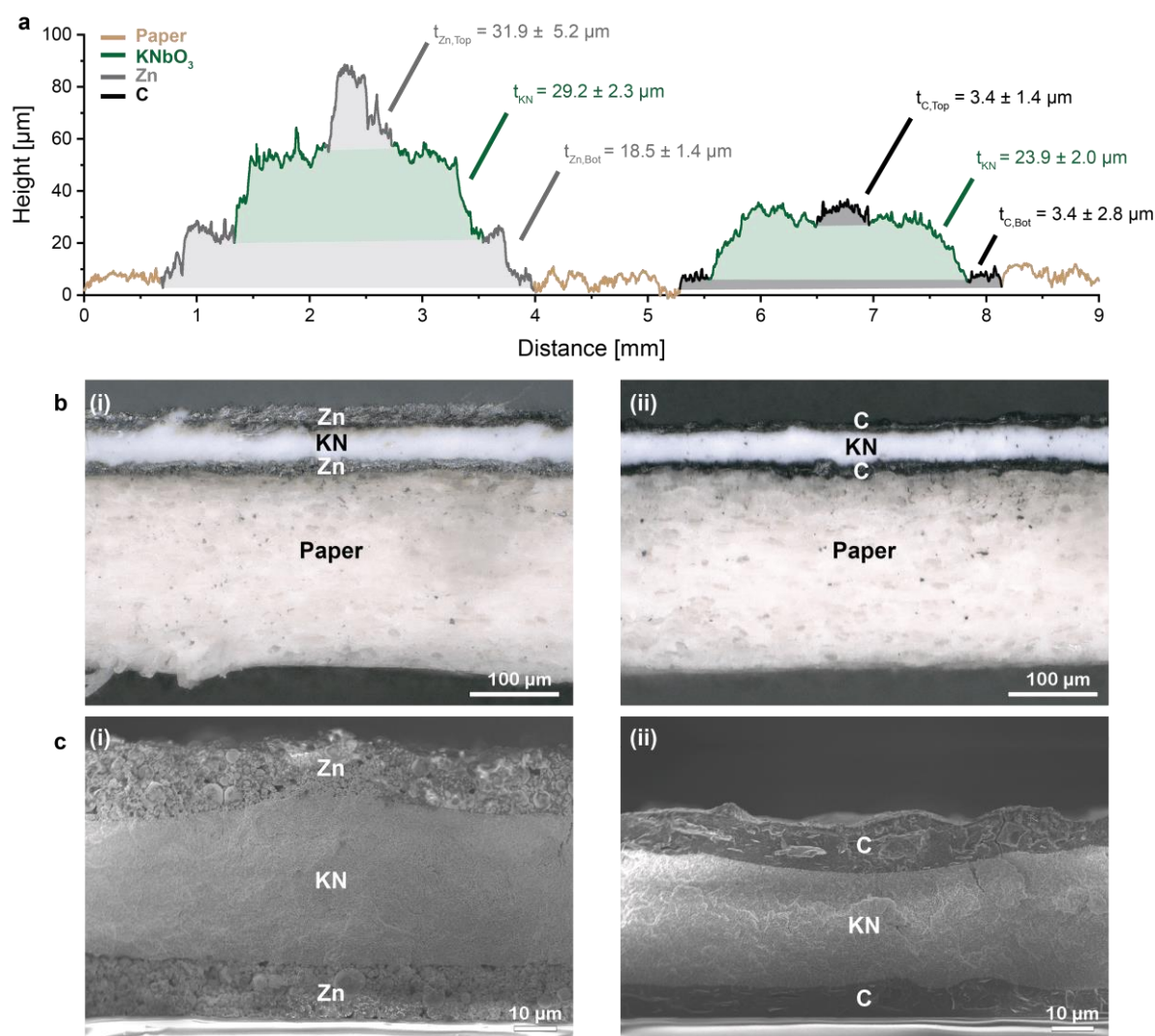

Figure 2. Physical characteristics of the fabricated devices. a) Surface profiles of the full device stacks for both zinc and carbon electrode devices, as measured on paper substrates. Profiles have been color coded to show approximate locations of the three device layers. b) Optical microscope images of devices cross section with (i) zinc and (ii) carbon electrodes, showing also the paper substrates and KN piezoelectric layers. c) SEM cross-sectional images of capacitor devices made with (i) zinc and (ii) carbon electrode materials, as imaged on glass substrates.

The bottom electrode layers were measured to be 18.5 ± 1.4 µm for zinc electrodes and 3.4 ± 2.8 µm for carbon bottom electrodes. The surface roughness values are comparable to that of the paper substrates, which was calculated to be 2.3 µm. The KN piezoelectric layer thickness was 29.2 ± 2.3 µm when printed on zinc electrodes, and 23.9 ± 2.0 µm when printed on carbon electrodes. The top electrodes had average thicknesses of 31.9 ± 5.2 µm and 3.4 ± 1.4

µm for the zinc and carbon layers respectively. This information is summarized along with other characteristic device parameters in **Table 1**.

Table 1. A comparison of relevant characteristics for piezoelectric devices fabricated using the different electrode materials.

Property	Units	Zinc Electrodes	Carbon Electrodes	Gold Electrodes
Eco-friendliness	[-]	Biodegradable	Biodegradable	Inert
Rel. Material Cost	[-]	Cheap	Cheap	Expensive
Deposition Method	[-]	Screen Printing	Screen Printing	Thermal Evaporation
Electrode Conductivity[a]	S m^{-1}	5×10^6	98 ± 21	4.55×10^7
Bottom Electrode Thickness[b]	µm	18.5 ± 1.4	3.4 ± 2.8	~ 0.1
Piezoelectric Layer Thickness[b]	µm	29.2 ± 2.3	23.9 ± 2.0	27.6 ± 1.3
Top Electrode Thickness[b]	µm	31.9 ± 5.2	3.4 ± 1.4	~ 0.1
$\varepsilon_{r,eff}$	[-]	14.6 ± 0.6	23.1 ± 0.1	22.3 ± 0.8
$d_{33,eff,max}$	pC N^{-1}	5.1 ± 0.8	4.6 ± 0.2	11.6 ± 0.8

Overall, the thickness of the piezoelectric layer was found to be highly consistent regardless of electrode material, with each successive print deposition adding approximately 4-5 µm of KN, resulting in a final layer thickness 20-30 µm after 6 depositions. The printed carbon layers were significantly thinner than the zinc layers, and showed consistent thickness between the top and bottom electrode layers. The thicknesses of the top and bottom zinc electrodes showed larger deviation, with the top electrodes being, on average, over 70% thicker than the bottom electrodes. Additionally, the average surface roughness of the zinc top electrodes was more than twice that of the bottom electrodes. This change in electrode layer thickness and surface roughness are attributed to the variance in sintering parameters implemented between the top and bottom zinc electrodes.

---

[a] Conductivity for gold taken as the conductivity of bulk gold.[33] Conductivity of zinc as reported by Fumeaux.[24]
[b] All layer thicknesses as reported when measured on paper substrates. Standard deviations represent calculated average surface roughness values. Gold electrode layer thicknesses assumed to be 0.1 µm based on thermal evaporation process parameters.

To further evaluate the morphological characteristics of these devices, optical and scanning electron microscopy (SEM) were utilized to inspect the interfaces between layers on each type of device. Optical microscopy images of the samples as printed on paper substrates are shown in Figure 3(b). The images show consistent layer thickness for all printed components, and support the profilometry measurements indicating the increased thickness of the zinc electrode layers as compared to the carbon electrodes.

Due to the nature of the cellulose fibers in paper, cross-sectional imaging of samples on paper was limited to optical observation, and thus, the SEM images below portray samples printed on glass substrates, not on paper substrates. As a result, the characteristics of the zinc top electrodes in this image may not fully represent the samples on paper, as the sintering parameters were not optimized for samples printed on glass substrates. Scanning electron microscopy of samples in cross-section are depicted in Figure 3(c) for samples with (i) zinc and (ii) carbon electrodes, showing the full device stacks as printed on glass substrates. Figure 1(b) and (c) depict the KN-electrode interfaces in greater detail. Inspection of the KN-top electrode interface shows excellent conformation for samples with carbon electrodes, however the interface for samples with zinc electrodes is less consistent, as the spherical nature of the zinc particles in combination with their variable size (ranging from $0.1 - 5$ µm), results in a less consistent interfacial area (See additionally Supporting Information Figure S3.1 and Figure S3.2). Further observation indicates that the top electrode zinc particulate near to the Zn-KN interface (deeper into the sample) may not have been fully sintered in the post-printing treatment process. This is most likely attributed to the directional nature of the photonic sintering step, which imparts the greatest energy on the exterior, exposed surface of the zinc layer before diffusing through to the lower portions of the layer. As previously discussed, the photonic sintering parameters were limited to mitigate the damaging effects of this high energy pulse on the lower layers of the device, it is possible that the identified parameters were sufficient to sinter the exposed surface of the top zinc electrode, but not the lower parts. To establish the validity of this hypothesis, and to evaluate the significance of its effects on the printed devices, further studies must be conducted, with more attention paid to this Zn-KN interface.

2.2.2. Dielectric and Piezoelectric Characteristics

The simple parallel plate capacitor design used in this investigation facilitated the evaluation of the dielectric characteristics of the devices, including the determination of the effective

relative permittivity for the piezoelectric layers according to a parallel plate capacitor assumption as follows **Equation 1.**

$$C = \left(\frac{A}{h_{piezo}}\right)\varepsilon_r\varepsilon_0 \tag{1}$$

where C is the measured device capacitance, A is the surface area of the printed capacitor, h_{piezo} is the thickness of the printed layer, ε_0 is the vacuum permittivity ($\varepsilon_0 = 8.854\ pF\ m^{-1}$), and ε_r is the relative permittivity of the printed layer.

Impedance and phase spectra were taken in the range of 1 kHz to 1 MHz at 1 V for samples with effective surface areas ranging between 5 and 30 mm^2 for all device types. **Figure 4**(a) and (b) show these spectra for samples of area 10 mm^2 of all types. The impedance spectra for these devices deviated from ideal capacitor behaviour, indicating that there was some electrical leakage present in the capacitor system in all cases. From these spectra, the device permittivity was calculated, using capacitance data extracted at 100 kHz (selected in lieu of the conventional 1 kHz parameter to reduce the influence of ambient humidity on the hygroscopic KN layer at lower frequencies). In Figure 4(c), we compare the capacitance measured versus the capacitor area, with annotations of the calculated relative permittivity of the devices as calculated from this information. The samples with gold and carbon electrodes showed nice agreement, with relative permittivity values of 22.3 ± 0.8 and 23.1 ± 0.1 respectively. However, the calculated value for the relative permittivity of the zinc electrode samples was notable calculated as just 14.6 ± 0.6, despite all samples being fabricated with close attention to consistent processing of the piezoelectric layers (both in terms of material used and layer thickness). This variance represents a reduction of approximately 37% in devices with zinc electrodes when compared to devices with gold or carbon electrodes. This could most likely be attributed to either a reduced electrode surface area for the zinc samples, as evidenced by the inconsistent interface between the KN and Zn layers in the cross-sectional images (Figure 3(d)), or to incomplete reduction of the oxide layer in the zinc top electrode, resulting in a double layer capacitor where the stack is comprised of Zn-ZnO$_x$-KN-Zn layers. As both steps of the zinc sintering process necessarily affect the top, exposed surface of the printed Zn layer before progressing through the interior. Hence, while the external surface of the top electrode is conductive, it is possible that the acid does not permeate sufficiently through to reduce the passivation layer on the particulate near the Zn-KN interface, or more likely, that the energy imparted during photonic process was only sufficient to sinter the top few microns of the printed electrode layer and not the full depth of it. Either condition, or a

combination thereof, would result in a mixed device stack with a $Zn-ZnO_x-KN-Zn$ mixed stack instead of the assumed $Zn-KN-Zn$ device intended. Further studies are necessary to diagnose the source of this atypical behavior.
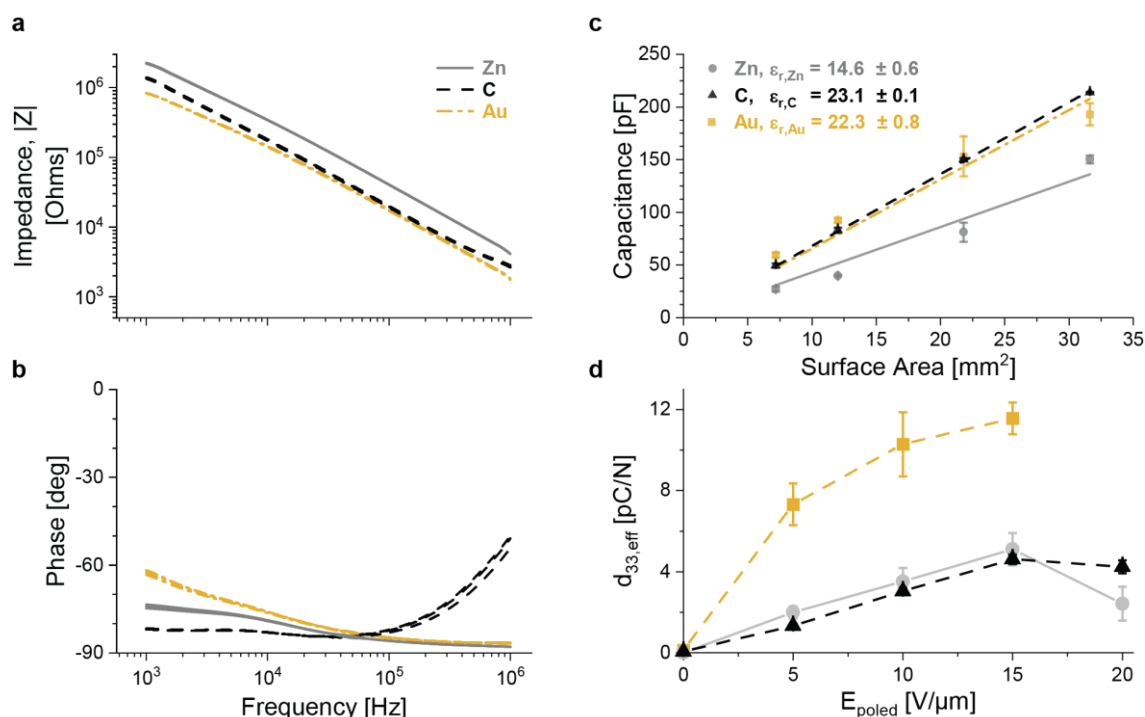

Figure 3. Electrical behavior of piezoelectric devices. a) Impedance and b) Phase spectra for devices fabricated with the varying electrode materials. c) Device capacitance as a function of capacitor surface area, with annotated effective relative permittivities, ε_r, for each device type. d) Piezoelectric coefficient, $d_{33,eff}$, as a function of applied field at poling.

Following dielectric analysis, the printed capacitors were poled to attain a piezoelectric response via direct (contact) poling. As the Curie temperature of KN ($T_{Curie,KN} = 225\ °C$) surpasses the thermal budget of the paper substrates ($T_{Max,Paper} \approx 150\ °C$), the conventional technique of poling at the ferroelectric material phase transition temperature could not be implemented. Thus, all samples were instead poled at ambient temperature. The applied poling field was varied in the range from $0 - 20\ V\ \mu m^{-1}$, as a means of evaluating the influence of electrode layers on the effective piezoelectric coefficient of the resulting devices, $d_{33,eff}$, when poled in ambient conditions. In line with the results of previous investigations on low temperature contact poling, the poling duration was fixed for all samples to be 5 min.[21] Supplementary Information Figure S4.1 provides more information on the poling process. The results of this study are depicted graphically in Figure 4(d). The magnitude of the piezoelectric response for the reference samples with gold electrodes match well with prior studies on this piezoelectric, with a maximum of $11.6 \pm 0.8\ pC\ N^{-1}$ when poled at $15\ V\ \mu m^{-1}$

(compared to 13.6 ± 2.8 pC N^{-1} reported previously).[21] Samples with gold electrodes were not evaluated for piezoelectric coefficients when poled at 20 V μm^{-1} due to breakdown events resulting in damage to the electrodes. A maximum piezoelectric response was obtained for samples poled with an applied field of 15 V μm^{-1} for samples with zinc or carbon electrodes, where the average effective piezoelectric coefficient was 5.1 ± 0.8 pC N^{-1} for zinc electrode devices and 4.6 ± 0.2 pC N^{-1} for carbon electrode devices.

The significant reduction in effective piezoelectric response for samples with the printed electrodes may potentially be explained by the presence of the thick electrode layers themselves. That is to say, the presence of significantly thick electrodes of either Zn or C may mechanically constrain the transducer stack, thereby limiting its displacement and thus reducing the observed piezoelectric coefficient. Future works should evaluate the source of this reduced performance, and look to mitigate the effects. This could be achieved, for example, through thinner electrode layers, or modifying the recipe used in the electrode inks, to adjust the stiffness of the resulting printed layer.

2.3. Sensing Demonstration: Force Sensor

As a means of demonstrating the practical application of this technology platform for sensing applications, we have used the described process to manufacture fully degradable paper-based force sensor grids, with devices made using both zinc and carbon electrodes.

The fabrication of these devices follows the same procedure as aforementioned, using an altered device design to produce a matrix of piezoelectric capacitors in a 4x4 grid pattern. The active area of each device was selected as 50 mm^2, intended to match the approximate size of a human fingertip as would be appropriate for future touch sensing applications. **Figure 5**(a) depicts a schematic of this design, and Figure 5(b) shows a photograph of a fully realized sensor, as fabricated with carbon electrodes.

Individual capacitors were poled using a poling field of 15 V μm^{-1} and a soak duration of 5 min, following the poling conditions determined previously to maximize the piezoelectric response of the samples (See Figure 4(d)). The $d_{33,eff}$ coefficient of each sample was measured using the Berlincourt method prior to force sensor characterization as a form of comparison. The measured piezoelectric coefficient for the devices studied was 6.0 ± 0.3 pC N^{-1} for samples with Zn electrodes, and 4.6 ± 0.2 pC N^{-1} for samples with carbon electrodes.

12

Figure 5(c) depicts a schematic of the measurement setup used in this evaluation. A vertical translation stage was used to compress the device as the applied force and voltage response were recorded. Figure 5(d) shows the resulting data, with the measured force (i) and voltage (ii) plotted as a function of time for samples with zinc or carbon electrodes (detailed information on the test protocol is available in Supporting Information Figure S5.1). The resulting measurements show a clear trend with increasing applied force producing an appropriately increasing voltage measurement under controlled measurement conditions.

The impedance of the devices and the input impedance of the voltmeter were next used to correlate the measured voltage with the corresponding charge according to **Equation 2** below and the responsivity of the devices was calculated through a correlation of the charge measured as a function of force applied (See Figure 5(e)).

$$q = \frac{1}{Z_L} \int V \, dt \tag{2}$$

Where q is the calculated charge, Z_L is the load impedance of the device under test, V is the measured output voltage, and t is time. From this study, the responsivity of the device with zinc electrodes was calculated as 10.5 pC N^{-1} while the responsivity of the device with carbon electrodes was 20 pC N^{-1}. The change in responsivity despite seemingly equivalent voltage response (as observed in Figure 5(d)) results from the load impedance (Z_L) of the two devices, with the zinc electrode device having a parallel resistance nearly double that of the carbon electrode sample (7 MΩ as opposed to 5.4 MΩ).

Figure 5(e) shows the clear presence of hysteresis in the carbon electrode samples, as evidenced by the varied sample response as the applied force is cycled.
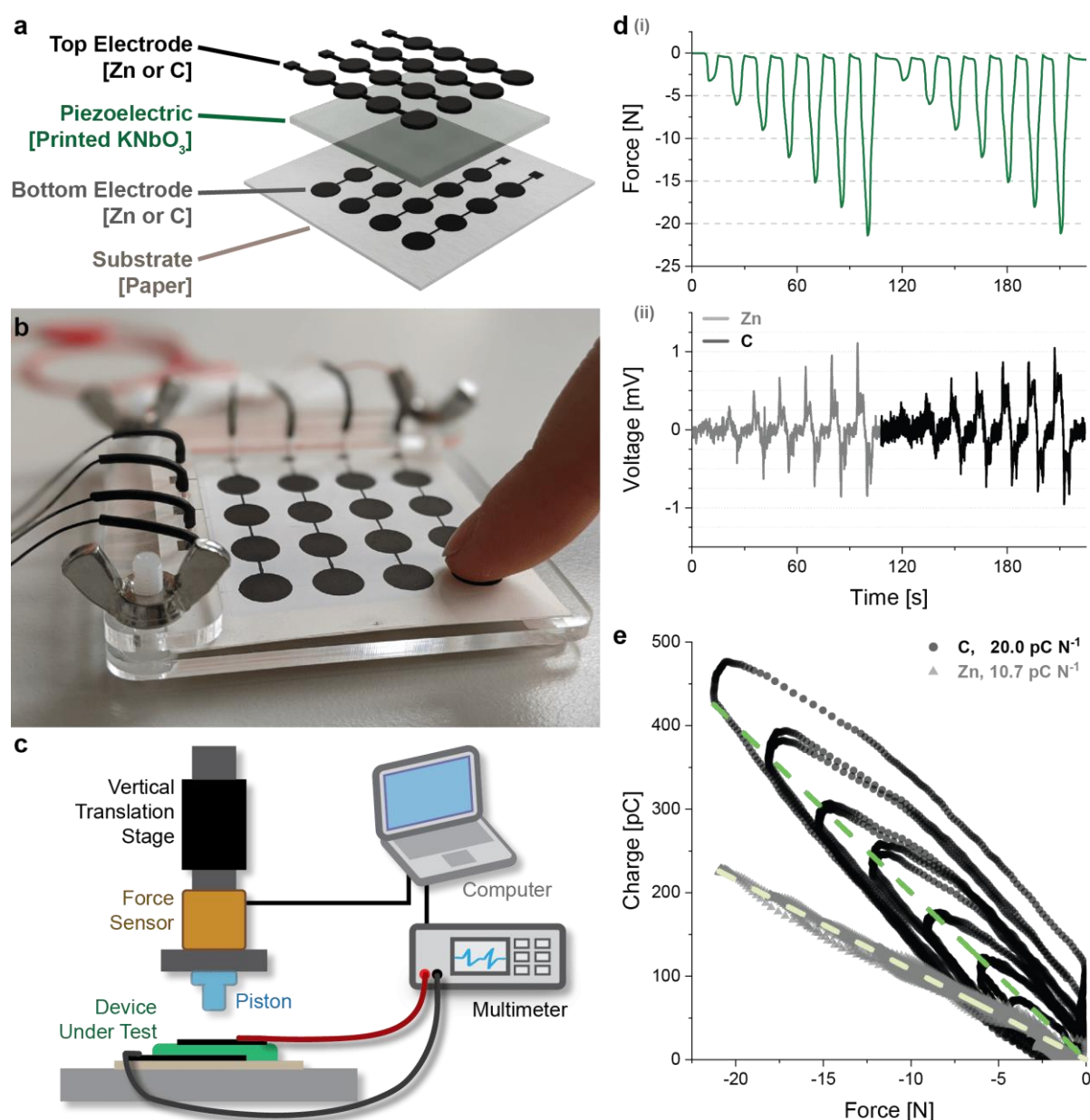
Figure 4. Fabrication and characterization of a fully printed degradable force sensor grid. a) Schematic depicting the design components. b) Photograph of the realized device, as fabricated using carbon electrodes. c) Schematic of the test setup for response characterization. d) (i)Force and (ii) voltage data collected during the measurement, showing the response of both sample types as the maximum applied force is increased. e) Charge as a function of applied force depicted for capacitor devices with zinc or carbon electrodes, with annotated device responsivities.

With device responsivities determined, a matrix of such devices could be utilized to determine force applied by measuring the output voltage from a practical implementation. Supporting Information Video SV1 demonstrates one such implementation, involving the transmission of a message via Morse Code using this device.

14

Future improvements of these systems will look to improve the signal of these force sensors, and work to correct any signal distortions caused by conflating factors such as sample heating or variations in ambient humidity conditions.

2.4. Actuating Demonstration: Acoustic Speaker

By exploiting the inverse piezoelectric effect, we demonstrate the potential for this technology in an actuating application through the development of a printed degradable speaker. While prior works have demonstrated the potential for printed piezoelectrics in acoustic applications, none have yet realized a fully degradable piezoelectric speaker, much less one with such adaptability as provided by printed electronics.[25–28] We elected to demonstrate this through the development of a speaker driver, which was even further implemented into biodegradable pair of personal headphones.

In **Figure 6**(a), we depict the fully assembled headphones, with an inset describing the buzzer inside the device. All components including all adhesives, all contact wires, the headphone body, and the ear cushions were made from eco-friendly materials, as detailed in the Methods section. The piezoelectric buzzer was comprised of the previously fabricated printed capacitor structures, integrated onto a cardboard backing plate, and sealed below a paper membrane (implemented to improve acoustic coupling). These buzzers were then evaluated for their acoustic response before being integrated into the 3D printed headphone body. A more detailed depiction of the assembly process can be found in Supporting Information Figure S6.1 and Figure S6.2.

Figure 6(b) shows a schematic depiction of the acoustic test chamber utilized to evaluate the response, including the mounted buzzer, recording microphone, and periphery electronics used to conduct testing. Figure 6(c) shows the recorded audio waveform as the speaker is cycled between an On and Off state of actuation at 10 kHz. The increase in response as the speaker is turned on is qualitatively significant.
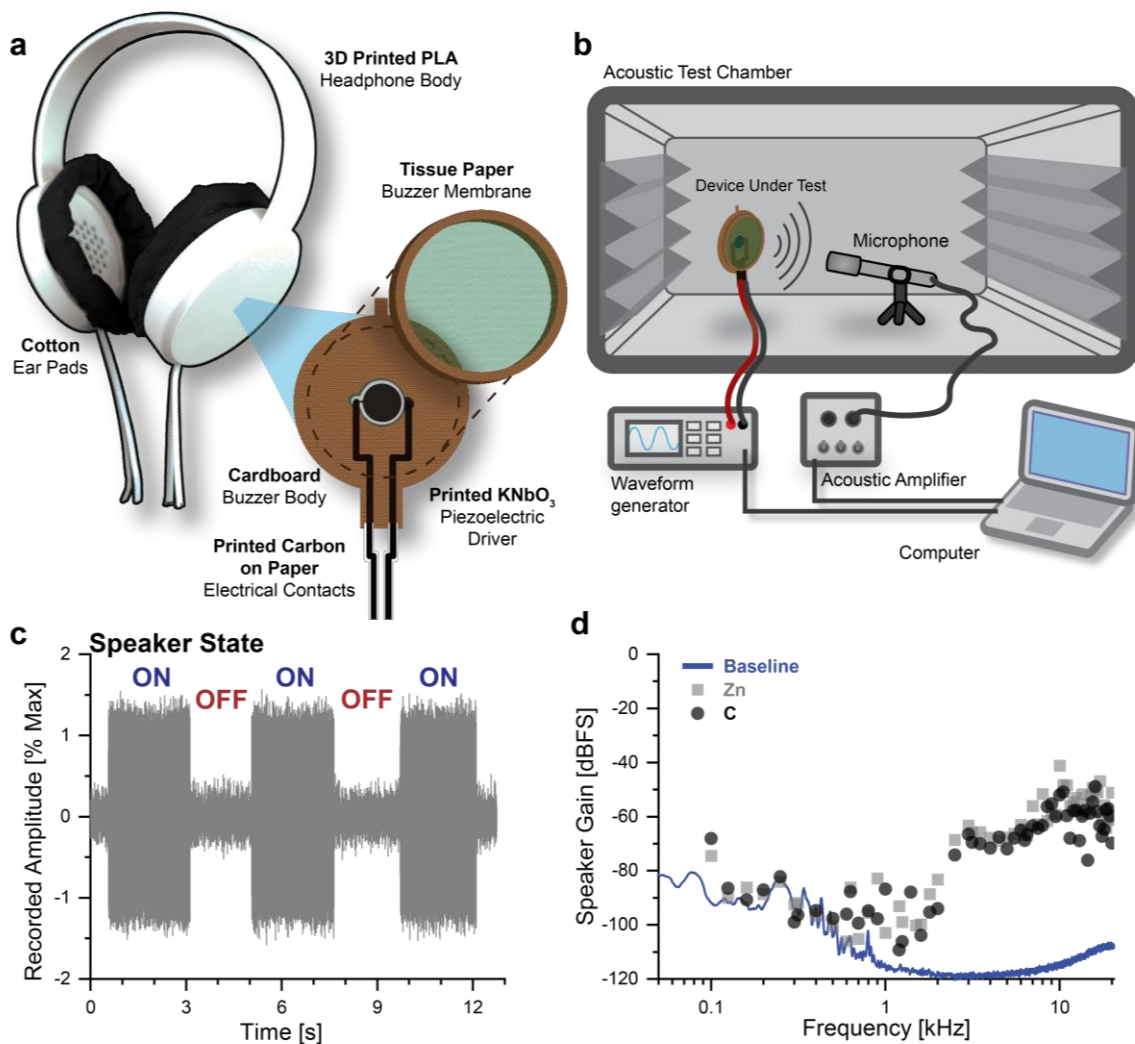
Figure 5. Fully degradable headphones demonstration. a) A schematic showing the final headphones, including the 3D printed chassis as well as the screen printed, biodegradable acoustic driver. b) A schematic of the test environment used to evaluate speaker response. c) Recorded signal amplitude as the speaker is cycled on and off, when actuated at 10 kHz. d) Acoustic periodogram showing response of speakers as a function of frequency relative to the ambient baseline noise level.

As a means of further quantifying the response of speakers, the relative sound amplitude at set discrete frequencies was measured and compared to the ambient noise floor of the testing environment. The resulting periodogram is plotted in Figure 6(d). Though the speaker response for both zinc electrode and carbon electrode buzzers was difficult to evaluate in the frequency range below 1 kHz, both types of devices showed a significant gain in the range from 2 – 20 kHz, being around 40 dB above the baseline in this frequency range. The periodogram further depicts a reasonably flat response in this frequency range, as is traditionally desirable for acoustic applications.

Supporting Information Figure S6.3 includes Laser Doppler Vibrometry data depicting the displacement of the buzzer membranes over the range from 0.1-20 kHz. Supporting Media Files SA1, SA2, and SA3 include several audio files recorded from these devices.

The simple architecture of this demonstrator shows great promise for biodegradable acoustic devices. Further optimization of both the printed piezoelectric capacitor shape as well as the housing design could provide significant improvements in acoustic performance. Future works will look to evaluating the progress that could be made to increase the speaker gain, particularly in the low frequency range, as well as evaluate methods to improve device efficiency at low actuation voltages to be compatible with conventional sound systems. In this sense, the adaptability and flexibility of a fully printed piezoelectric platform opens the door to novel architectures for piezoelectric drivers, a deviation from the current conventional drives which are constrained to simple disk shapes not optimized for all acoustic applications.

3. Conclusion

In this work, a process was developed to manufacture the first ever instances of fully printed degradable piezoelectric microsystems, through the integration of printed degradable conductors with a printed piezoelectric layer comprised of potassium niobate, $KNbO_3$, processed at low temperature on paper substrates. The process was established for two different degradable conductive inks, one utilizing carbon, and another utilizing zinc as the primary conductive components, and involved adapting the different printed layers to realize fully printed piezoelectric devices. The optimized process achieved a high fabrication yield of homogeneous devices, with printed active surface areas as large as 60 mm^2. Device characterization and analysis showed the viability of both zinc and carbon printed layers for use as degradable electrodes in KN based piezoelectric systems. Piezoelectric performance with the printed electrode was optimized for each type of device as a function of poling field, achieving effective piezoelectric coefficients of 5.1 ± 0.8 pC N^{-1} with zinc electrodes and 4.6 ± 0.2 pC N^{-1} with carbon electrodes. This investigation culminated with the manufacture of two types demonstrator devices, one each to highlight the sensing and actuating potential of the technology through the direct and inverse piezoelectric effect respectively. A matrix of force sensors was fabricated using both zinc and carbon electrode materials, and the response of each determined in the typical force range for touch sensing applications. Taking advantage of the actuating capability of the printed piezoelectric devices, we have demonstrated the first-ever acoustic speaker system fully made of degradable materials, including both the

piezoelectric sound driver as well as an eco-friendly 3D printed headphone casing. Speaker drivers comprised of printed KN piezoelectric capacitors using either zinc or carbon electrodes in paper housings were evaluated for their acoustic performance in the auditory range of 50 Hz – 20 kHz. Drivers with both electrode types showed peak performance in the range from 2-20 kHz, showing a relative gain of 40 dB above the ambient noise level, and with an open door for improved performance as designs are optimized for acoustic applications. Future developments would aim to improve the piezoelectric performance of the printed devices, as well as integrate this technology into more advanced forms of printed MEMS devices. This work paves the way for future implementation of such processes towards higher complexity and more sustainable piezoelectric devices and systems.

4. Methods

Materials: All printed piezoelectric devices were fabricated on ArjoWiggins PowerCoat XD 200 screen printing paper (200 μm thickness, 219 g m^{-2}). For samples used in SEM imaging, samples were printed on glass wafers (Borofloat 33, 100 mmØ, 500 μm thickness, Siegert Wafer GmbH).

The Cr/Au (10/100 nm) gold reference electrodes were thermally evaporated using a Leybold L560 thermal evaporator using shadow masks fabricated from 200 μm thick stainless steel by Beta-Layout GmbH.

The carbon ink utilized was BareConductive Electric Paint (SKU-0216), a water based, screen printable carbon ink utilizing natural resin as the adhesive ingredient.

The zinc conductive ink was prepared using following components: Zn powder (CAS 7440-66-6, US Research Nanomaterials Ink., 500 nm average diameter, 99.9% (metal basis)), polyvinylpyrrolidone (CAS 9003-39-8, Merck, MW=360K), and 1-pentanol (CAS 71-41-0, Merck, ReagentPlus, ≥99%).

The piezoelectric ink was prepared using the following components: $KNbO_3$ powder (CAS 12030-85-2, Alfa Aesar Puratonic 99.999% (metal basis)), ethyl cellulose (CAS 9004-57-3, Merck, viscosity 10 cP, 5% in toluene/ethanol 80:20 (lit.), extent of labelling: 48% ethoxyl), and 1-pentanol (CAS 71-41-0, Merck, ReagentPlus, ≥99%). All component materials are recognized as non-toxic, with potential for sustainable production.[29–32]

Preparation of Zn-based ink: The ink ingredients were mixed in a weight ratio of 25:1:5 Zn:PVP:1-pentanol. The ink was homogenized with a planetary mixer (Thinky ARE-250) at 300 rpm for 30 minutes. Three stainless steel mixing balls of 8 mmØ were used as mixing

media. The ink was stored at 4 °C in a well-sealed container. Prior to printing, the ink was re-homogenized at 500 rpm for 10 minutes in the planetary mixed and printed once at ambient temperature.

Preparation of KNbO₃-based ink: Prior to ink manufacture, the KN powder was ground in order to reduce average particle diameter and improve the homogeneity of the particle sizing, following the procedure previously described by Monroe.[21] Five grams of KN powder was placed in a Teflon grinding vessel (72 mL volume, fabricated in-house), along with 10 mL of 1-propanol and 125 g of ZrO_2 grinding media (2 mmØ, Retsch). Grinding was conducted in a planetary ball mill (QM-3SP2), for a total duration 24 hrs, with a directional switching period of 0.3 hrs and a jar rotational speed of 200 rpm. Once complete, the powder was separated from the media, dried, and finally annealed in a furnace (Thermolyne F6020-33-80 Tabletop muffle furnace) at 625 °C for 4.5 hrs followed by passive cooling for approximately 16 hrs to ambient temperature. The resulting powder showed a reduction in average particle size from nearly 4 μm in the unground powder to approximately 160 nm in the ground powder.
The ground KN powder was then mixed with ethyl cellulose and 1-pentanol in a proportional ratio of 58:7.5:35 wt.% KN:EC:1-pentanol. Ink mixing was conducted in the planetary mixer using 5 g of 5 mm Ø Al_2O_3 spherical milling media (Retsch). Mixing was conducted at 700 rpm in 30 min intervals to reduce solvent evaporation due to system heating. The total duration of mixing was 2 hrs. To adjust for the solvent lost due to heating, slight additions of 1-pentanol were required to attain the targeted ink viscosity. Once mixed, ink was stored at 5 °C in a well-sealed container. No re-homogenization was required for this ink prior to printing.

Manufacturing: Paper substrates were pre-cut via laser cutting using a Trotec Speedy 300 (60 W) laser cutter to a consistent size with engraved alignment marks to ensure a consistent process across all samples. No pre-treatments were required on paper substrates prior to further processing. For the samples printed on glass, the substrates were pre-treated using an O_2 plasma cleaned (Diener ATTO, 100% Power, 10 min). All paper substrates were clamped to a stiff polyoxymethylene carrier plate before initial printing to reduce substrate warping through successive processing steps.
A manual screen printer (Charmhigh 3040 High Precision Manual Solder Paste Printer) was used for printing all inks (carbon, zinc, and KN). Mesh fabrication was provided by Serilith AG (Balwil, CH) using polymer (PME 120-30Y) and steel mesh (SD 40/25) materials.

Carbon ink layers were dried for 12 hrs under ambient conditions. Zinc layers were dried for 30 min under ambient conditions prior to the post-printing treatment process detailed below. The KN ink layers were dried in a Memmert UF110plus oven at 120 °C for 30 min after each layer, for a total of 6 layers.

Post-printing treatment of zinc electrodes was conducted following Fumeaux, and consisted of the following two phases.[24]

The first phase consisted of chemical reduction of the ZnO passivation layer on individual Zn particles. Dilute acetic acid (CAS 64-19-7, Merck, 1M CH_3COOH, diluted to 10 vol% in deionized water) was spray-coated on the screen-printed Zn electrodes using an aerosolizing airbrush (Harder & Steenbeck, 0.2 mm nozzle) supplied by nitrogen gas (2 bar) at a distance of approximatively 10 cm from the sample surface. Each pass of spray was followed by a 5 min drying period on a hot plate at 50 °C. This spray-coating/drying cycle was repeated a total of 10 times. This process was conducted entirely under a fume hood. Once this phase was complete, samples were immediately transferred to the second phase of processing.

The second phase involved photonic sintering to melt the now-reduced Zn particles and produce a cohesive bulk layer of conductive zinc. Samples were first placed in an anaerobic environment, using a custom chamber adapted for the Novacentrix PulseForge 1200 photonic sintering instrument, to reduce the potential effects of Zn re-oxidation. The sealed chamber was purged with nitrogen for a minimum of 30 seconds prior to sintering. The photonic sintering treatment comprised pulse energies ranging from 6550 to 9900 mJ cm^{-2} and between 1 and 3 pulses were delivered. All recipes using in process optimization constrained pulse duration to 30 ms, with a pulse frequency of 0.1 Hz. Final recipes involved 3 pulses at 6550 mJ cm^{-2} for the bottom electrode zinc layer, and 1 pulse of 7550 mJ cm^{-2} for the top electrode zinc layer.

A programmable high voltage power supply (Peta-Pico-Voltron, developed in-house) was used for direct poling of finished devices. First, the devices were connected to the high voltage power supply. The applied voltage was then stepped up to the target value with ramp steps equivalent to 1 V μm^{-1} every 5 seconds, where the target voltage was maintained for a soaking period of 5 min before the applied voltage was removed (See Supporting Information Figure S4.1 for schematic), and the process completed. The applied electric fields targeted in the poling optimization were 0, 5, 10, 15, or 20 V μm^{-1}. The maximum applied electric field was constrained to 20 V μm^{-1} due to dielectric breakdown limitations.

Speaker Assembly: Cardboard backing (550 g m^{-2}), was laser cut to form the backing plate and membrane support rings for use in piezoelectric buzzers. The piezoelectric devices were then adhered to the backing plate using non-toxic polyvinyl acetate (PVA) adhesive. Electrical interconnects are then made between devices using the carbon ink via stencil printing. Ink drying occurred under ambient conditions for 30 min. The tissue membrane (20 g m^{-2}) was tensioned across a frame and adhered to the membrane support rings using the PVA adhesive. The membrane was then attached to the backing plate with the same adhesive and allowed to cure in ambient conditions for a minimum of 1 hr. The headphone chassis was 3D printed from non-toxic polylactic acid (PLA) filament using a Raise3D E2 dual-extruder FDM Printer. The 3D model was adapted from a design produced by Shannon Ley. The earphone cushions were hand-sewn using cotton fabric and natural cotton stuffing. Cushions were attached via natural cotton yarn in lieu of adhesive to allow for removal. The details of this process are depicted in Supporting Information Figure S6.2.

Device Characterization: Ink properties were analysed using a Keyence VHX Digital Microscope Series optical microscope, a JEOL JSM-7500TFE scanning electron microscope. Layer thickness and surface roughness measurements were conducted using an Ambios XP-2 profilometer. The dielectric properties were measured using a Digilent Analog Discovery 2 all-in-one test and measurement device with the Impedance Analyzer addition. Direct piezoelectric effect measurements were measured using an in-house Berlincourt meter courtesy of Prof. Dragan Damjanovic at EPFL. The meter showed a noise threshold $d_{33,eff}$ of approximately 0.05 pC N^{-1}, for which all measurements were appropriately compensated.

Force Sensor Characterization: Force sensor characterization was conducted using an Instron 3340 Single Column Universal Testing System mechanical setup. A piston mounted to the vertical translation stage was used to compress the device, while an in-line Futek 2519-50N force sensor measured the applied force in real time and an Agilent 34410A multimeter recorded the voltage response of the sample and recorded via a LabView script. Compressions were implemented following a force-controlled triangular waveform with a 10s compression and release cycle followed by a 5 s pause step at 0 N. Repetitions are made for sample compression from 5-20 N with an actuation frequency of 0.1 Hz. The parallel resistance of the devices was measured at 20 Hz using an Agilent E4980A Precision LCR meter. More detailed information can be found in Supporting Information S5.1.

Speaker Characterization: Speaker characterization was conducted using a Seinheiser MKH 416-P48U3 microphone via a Steinberg UR mk II USB Audio Interface. Speaker drivers were actuated using a Digilent Analog Discovery 2 via the waveform generator functionality, with a set signal amplitude of 5 V. All audio data was recorded via Audacity with a sampling rate of 44.1 kHz and processed in Origin. Laser Doppler vibrometry was conducted using a PolyTec MSV-400 microscope scanning vibrometer utilizing a VD-06 velocity decoder. To produce the periodogram data for each speaker, the following process was implemented. First, the samples were installed in the acoustic test chamber, at a distance of 10 mm from the recording microphone. With the chamber sealed, the ambient noise was recorded for a duration of 30 s to establish the environmental baseline noise level for the test. Next, the speaker was actuated at a discrete frequency between $0.1 – 20$ kHz, and the resulting audio recorded for a duration of 30 s. This process was repeated for a set of frequencies selected using a conventional A-weighting table. Each audio file was trimmed to be precisely 10 s in duration, and an FFT was taken of each. The speaker gain at each set test frequency could then be extracted from the corresponding FFT, and compared to the ambient baseline to establish the performance of the speaker.

Supporting Information

Supporting Information is available from the Wiley Online Library or from the author.

References

[1]   R. Kuehr, in *Waste Electrical and Electronic Equipment (WEEE) Handbook*, Elsevier, **2019**, pp. 1–16.

[2]   H. Nakamura, S. Suzuki, T. Tezuka, S. Hasegawa, K. Maruta, *Proceedings of the Combustion Institute* **2015**, *35*, 3397.

[3]   M. Schluep, C. Hagelueken, R. Kuehr, F. Magalini, C. Maurer, C. Meskers, E. Mueller, F. Wang, *Recycling - from e-Waste to Resources*, **2009**.

[4]   Q. Yang, T.-L. Liu, Y. Xue, H. Wang, Y. Xu, B. Emon, M. Wu, C. Rountree, T. Wei, I. Kandela, C. R. Haney, A. Brikha, I. Stepien, J. Hornick, R. A. Sponenburg, C. Cheng, L. Ladehoff, Y. Chen, Z. Hu, C. Wu, M. Han, J. M. Torkelson, Y. Kozorovitskiy, M. T. A. Saif, Y. Huang, J.-K. Chang, J. A. Rogers, *Nat Electron* **2022**, *5*, 526.

[5]   X. Yu, W. Shou, B. K. Mahajan, X. Huang, H. Pan, *Advanced Materials* **2018**, *30*, 1.

[6]   J. Li, J. Liu, W. Huo, J. Yu, X. Liu, M. J. Haslinger, M. Muehlberger, P. Kulha, X. Huang, *Mater Today Nano* **2022**, *18*, 100201.

[7]   M. J. Tan, C. Owh, P. L. Chee, A. Ko, K. Kyaw, D. Kai, X. J. Loh, *J Mater Chem C Mater* **2016**, *4*, 5531.

[8]   J. Rödel, W. Jo, K. T. P. Seifert, E.-M. Anton, T. Granzow, D. Damjanovic, *Journal of the American Ceramic Society* **2009**, *92*, 1153.

[9]   P. K. Panda, *J Mater Sci* **2009**, *44*, 5049.

[10] S. Khan, L. Lorenzelli, R. S. Dahiya, *IEEE Sens J* **2015**, *15*, 3164.

[11] G. Lau, M. Shrestha, *Micromachines (Basel)* **2017**, *8*, 194.

[12] K. Y. Mitra, A. Willert, R. Chandru, R. R. Baumann, R. Zichner, *Adv Eng Mater* **2020**, *22*, DOI 10.1002/adem.202000547.

[13] J. Chang, T. Ge, E. Sanchez-Sinencio, *Midwest Symposium on Circuits and Systems* **2012**, 582.

[14] M. R. Somalu, A. Muchtar, W. R. W. Daud, N. P. Brandon, *Renewable and Sustainable Energy Reviews* **2017**, *75*, 426.

[15] Y. Zhang, Y. Zhu, S. Zheng, L. Zhang, X. Shi, J. He, X. Chou, Z. S. Wu, *Journal of Energy Chemistry* **2021**, *63*, 498.

[16] S. Lambert, M. Wagner, *Chem Soc Rev* **2017**, *46*, 6855.

[17] D. L. Wen, D. H. Sun, P. Huang, W. Huang, M. Su, Y. Wang, M. di Han, B. Kim, J. Brugger, H. X. Zhang, X. S. Zhang, *Microsyst Nanoeng* **2021**, *7*, DOI 10.1038/s41378-021-00261-2.

[18] M. Irimia-Vladu, E. D. Głowacki, G. Voss, S. Bauer, N. S. Sariciftci, *Materials Today* **2012**, *15*, 340.

[19] C. Cointe, A. Laborde, L. G. Nowak, D. N. Arvanitis, D. Bourrier, C. Bergaud, A. Maziz, *Microsyst Nanoeng* **2022**, *8*, DOI 10.1038/s41378-022-00353-7.

[20] W. Li, M. Vaseem, S. Yang, A. Shamim, *Microsyst Nanoeng* **2020**, *6*, 77.

[21] M. M. Monroe, L. G. Villanueva, D. Briand, *Microsyst Nanoeng* **2023**, *9*, 19.

[22] A. Poulin, X. Aeby, G. Siqueira, G. Nyström, *Sci Rep* **2021**, *11*, 1.

[23] C. O'Mahony, E. U. Haq, C. Sillien, S. A. M. Tofail, *Micromachines (Basel)* **2019**, *10*, 99.

[24] N. Fumeaux, D. Briand, *npj Flexible Electronics* **2023**, *7*, 14.

[25] J. Han, M. Saravanapavanantham, M. R. Chua, J. H. Lang, V. Bulović, *Microsyst Nanoeng* **2022**, *8*, DOI 10.1038/s41378-022-00384-0.

[26] K. Y. Mitra, M. Polomoshnov, C. Martínez-Domingo, D. Mitra, E. Ramon, R. R. Baumann, *Adv Electron Mater* **2017**, *3*, 1700275.

[27] J. Kim, G. Y. Yun, J. H. Kim, J. Lee, J. H. Kim, *Journal of Mechanical Science and Technology* **2011**, *25*, 2763.

[28] R. Gao, X. Chu, Y. Huan, Y. Sun, J. Liu, X. Wang, L. Li, *Smart Mater Struct* **2014**, *23*, DOI 10.1088/0964-1726/23/10/105018.

[29] P. Beguin, J.-P. Aubert, *FEMS Microbiol Rev* **1994**, *13*, 25.

[30] A. M. Agrawal, R. V. Manek, W. M. Kolling, S. H. Neau, *AAPS PharmSciTech* **2003**, *4*, DOI 10.1208/pt040460.

[31] H.-C. Tseng, Production of Pentanol in Metabolically Engineered Escherichia Coli, **2011**.

[32] A. F. Cann, J. C. Liao, *Appl Microbiol Biotechnol* **2010**, *85*, 893.

[33] W. M. Haynes, D. R. Lide, T. J. Bruno, Eds., *CRC Handbook of Chemistry and Physics*, CRC Press, **2016**.